# An innovative physical scheme to retrieve simultaneously surface temperature and emissivities using high spectral infrared observations from IASI

M. Paul, F. Aires, Christophe Prigent, I.F. Trigo, Frédéric Bernardo

# An innovative physical scheme to retrieve simultaneously surface temperature and emissivities using high spectral infrared observations from IASI

M. Paul,[1,2] F. Aires,[3,4,5] C. Prigent,[1] I. F. Trigo,[6,7] and F. Bernardo[8,9]

Received 14 December 2011; revised 27 February 2012; accepted 23 April 2012; published 5 June 2012.

[1] Retrieving atmospheric temperature and water vapor profiles from infrared satellite observations over continental surfaces is a complex problem because of the heterogeneity of land surfaces and the difficulty of modeling their interaction with the radiation. This results in the surface-sensitive observations from sounding instruments over land usually not being assimilated into numerical prediction systems at meteorological operational centers. Correct characterization of the interaction between the atmosphere and the surface would allow considering the information contained in those channels. This requires accurate estimates of the surface emissivities at the spectral resolution of recent instruments such as Infrared Atmospheric Sounding Interferometer (IASI) or Atmospheric Infrared Sounder (AIRS). An emissivity interpolator is developed in this study to estimate the land surface emissivities at a high spectral resolution compatible with IASI or AIRS instrument channels. It is based on Moderate Resolution Imaging Spectroradiometer (MODIS) retrieved emissivities. This surface emissivity is used as a first guess in an innovative surface parameter inversion scheme that simultaneously retrieves the surface emissivity and temperature. Radiative transfer calculations with the resulting surface information show a significantly better agreement with the observations (root mean square error of 1.7 K on average over bands 1 and 2 of the IASI spectrum), as compared to calculations using the first guess information (root mean square error of 3.5 K). The retrieved surface skin temperatures are compared to the Land Surface Analysis Satellite Applications Facility (LSA SAF) estimates derived from Spinning Enhanced Visible and Infrared Imager (SEVIRI) measurements, and the root mean square difference is below 2 K.

**Citation:** Paul, M., F. Aires, C. Prigent, I. F. Trigo, and F. Bernardo (2012), An innovative physical scheme to retrieve simultaneously surface temperature and emissivities using high spectral infrared observations from IASI, *J. Geophys. Res.*, *117*, D11302, doi:10.1029/2011JD017296.

## 1. Introduction

[2] Satellite retrieval of key atmospheric variables close to the surface is limited by our knowledge of the surface characteristics: The signal measured by the satellite is the sum of atmosphere and surface terms and it is difficult to disentangle these two contributions. Two key parameters drive the surface contribution to the measured radiance: The surface temperature and emissivity. It is essential to improve our knowledge of these two parameters to increase atmospheric retrieval accuracy, especially in the lower atmospheric layers. The problem is more challenging over land than over ocean: First, the surface skin temperature is much more variable over land than over ocean, with large amplitudes of the diurnal cycle especially in arid and semi-arid regions; second, the emissivity is also much more variable over land due to the heterogeneity of surface characteristics such as soil nature, presence of vegetation, moisture, or snow.

[3] Lately, significant efforts have been carried out, both in the infrared [e.g., *Yu et al.*, 2008] and in the microwave [e.g., *Aires et al.*, 2011a], to estimate the land surface emissivities, in order to improve the retrieval of surface

[1]Laboratoire de l'Etude du Rayonnement et de la Matière en Astrophysique, CNRS, UPMC, Observatoire de Paris, Paris, France.
[2]Also at Laboratoire de Météorologie Dynamique, IPSL, CNRS, Université de Paris VI, Jussieu, France.
[3]Estellus, Paris, France.
[4]Also at Laboratoire de Météorologie Dynamique, IPSL, CNRS, Université de Paris VI, Jussieu, France.
[5]Also at Laboratoire de l'Etude du Rayonnement et de la Matière en Astrophysique, CNRS, UPMC, Observatoire de Paris, Paris, France.
[6]Instituto de Meteorologia, Lisbon, Portugal.
[7]Also at IDL, University of Lisbon, Lisbon, Portugal.
[8]Laboratoire de Météorologie Dynamique, IPSL, CNRS, Université de Paris VI, Jussieu, France.
[9]Also at Laboratoire de l'Etude du Rayonnement et de la Matière en Astrophysique, CNRS, UPMC, Observatoire de Paris, Paris, France.

Corresponding author: M. Paul, Laboratoire de l'Etude du Rayonnement et de la Matière en Astrophysique, Observatoire de Paris, 61 ave. de l'Observatoire, Paris F-75014, France. (maxime.paul@obspm.fr)


0148-0227/12/2011JD017296

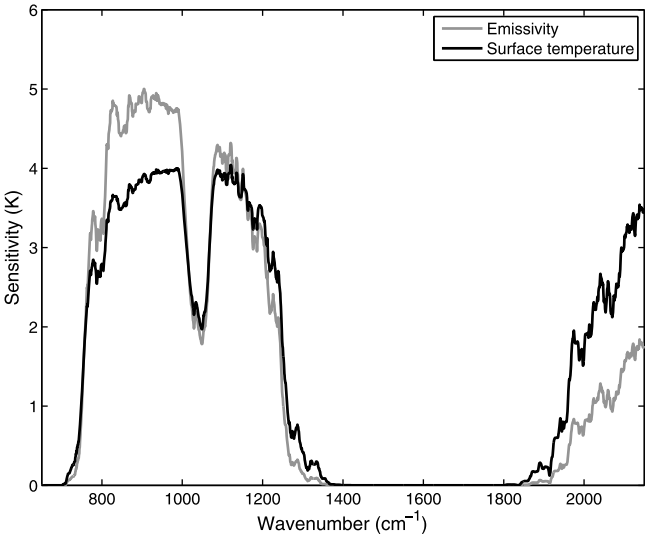


**Figure 1.** Mean sensitivity of Infrared Atmospheric Sounding Interferometer (IASI) channels to a perturbation of 5 K in surface temperature (in black) or 0.1 in emissivity (in grey) over land. The calculation has been performed over a sample of 100,000 different situations. A running mean over 10 channels has been used for this figure in order to smooth the curve.

temperature and atmospheric profiles in the lower atmospheric layers [*Aires et al.*, 2011b]. This study focuses on the infrared domain, where the recent availability of observations at very high spectral resolution from Infrared Atmospheric Sounding Interferometer (IASI) or Atmospheric Infrared Sounder (AIRS) (see section 2.1) imposes the development of high spectral resolution emissivity databases to fully benefit from the surface-sensitive channels, in research and operational modes.

[4] Two types of emissivity retrieval methodologies can be considered. A first family of retrieval schemes uses an empirical approach: a "learning data set" built with satellite measurements and associated emissivities. It is used to calibrate a statistical model (regression or neural network) designed to estimate the emissivity. This type of approach has been used in the microwave domain [e.g., *Aires et al.*, 2001] or in the infrared [e.g., *Zhou et al.*, 2011]. The second family of retrieval schemes uses a physical approach: Radiative transfer computations are involved in the retrieval scheme [*Pequignot*, 2006; *Prigent et al.*, 2006]. The empirical approach has the advantage to be very fast in operational mode contrarily to the physical strategy. However, when the physical problem is too complex, some of the parameters can be difficult to take into consideration. For instance, aerosols over the Saharan desert would contaminate the empirical retrievals if not explicitly and accurately included within the training process. In the physical retrieval schemes, aerosol or cloud information for example, can be integrated more easily. As a consequence, in this study, we will combine the two retrieval strategies.

[5] Various land surface emissivity data sets have been developed recently to serve as first guesses in the inversion of infrared sounder observations. For instance, *Seemann et al.* [2008] developed a high-resolution emissivity data set based on an interpolator scheme that retrieves high-resolution emissivity spectra compatible with instruments like IASI or AIRS: It is based on a limited number of broadband emissivities from the Moderate Resolution Imaging Spectroradiometer (MODIS) instrument. The fact that these emissivity first guesses result from MODIS and are totally independent from the IASI or AIRS observations is an advantage for the retrieval scheme: The first guess and the satellite observations are supposed to be independent in the variational assimilation framework [*Rodgers*, 2000]. The principle of anchoring an interpolation scheme to a reference emissivity data set has been exploited in the microwave as well [*Prigent et al.*, 2008; *Aires et al.*, 2011a].

[6] Radiative transfer calculation of the sensitivity of the IASI channels to changes in surface temperature and emissivities (Figure 1) confirms that brightness temperatures in the infrared are highly sensitive to both parameters. It provides a first estimation of the relative importance of the two parameters [*Hulley and Hook*, 2009]. The requirements for current instruments is to retrieve the surface temperature with a root mean square error of 1 K: This is not reached yet. This is equivalent to a precision of $2 \times 10^{-2}$ for the surface emissivities. As a consequence, the retrieval of the emissivities, and more generally, the estimation of the surface contribution to the satellite signal requires a surface temperature of good quality [*Vogel et al.*, 2011]. Conversely, an error in the surface temperature can be compensated by an error in the emissivity. It is recommended to retrieve these two variables simultaneously. This has been done in the microwave [Aires et al., 2001], and in the infrared [*Wan and Li*, 1997].

[7] In this study, the goal is to capitalize on all these recent developments in both the infrared and microwave domains and to develop an efficient and innovative global approach for IASI, by combining the two approaches: empirical (the interpolator) and physical (the retrieval itself). First, a high-resolution infrared emissivity interpolation tool is built based on a reference emissivity data set from MODIS. It provides a high quality coherent emissivity first guess (the error of the interpolatoris below $4 \times 10^{-3}$) for the subsequent retrieval scheme. A physical algorithm is then designed to retrieve simultaneously the surface temperature and emissivities at IASI spectral resolution.

[8] The different data sets used in this study are first presented (section 2). Section 3 presents the high spectral resolution infrared emissivity interpolator that provides the first guess to the retrieval scheme. The surface temperature and emissivity retrieval scheme is described in section 4, together with some evaluation. Finally, the results of the retrieval algorithm are presented in section 5. Conclusions and perspectives are provided in section 6.

## 2. Data Sets and Tools

[9] First, the infrared IASI observations are described. Second, the existing infrared land surface emissivity databases are presented, in particular the MODIS UCSB (University of California, Santa Barbara) and the Advanced Spaceborne Thermal Emission and Reflection (ASTER) library that are the basis for the emissivity interpolator. The other ancillary data sets, the European Centre for Medium-range Weather Forecasts (ECMWF) analysis, the International

Geosphere-Biosphere Programme (IGBP) surface classification and a monthly snow information database are briefly introduced. A brief description of the radiative transfer tool is also provided.

### 2.1. IASI Observations

[10] MetOp is a series of three meteorological operational satellites in polar orbit developed by the European Space Agency (ESA). The first one has been launched on 19 October 2006. It orbits at 840 km above the Earth, it takes 101 min and it is Sun-synchronous. It includes twelve instruments for meteorological applications. This study focuses on the measurements from the Infrared Atmospheric Sounding Interferometer (IASI) [*Chalon et al.*, 2001]. It represents half the data provided by MetOp. It consists of 8461 channels equally distributed between 645 and 2760 $cm^{-1}$. The measurement technique is based on an accurately calibrated passive infrared spectrometer with Fourier transformation. IASI observes in three bands: band B1, from 645 to1210 $cm^{-1}$; band B2, from 1210 to 2000 $cm^{-1}$; and band B3, from 2000 to 2 760 $cm^{-1}$. Band B3 has a very low signal-to-noise ratio and can hardly be exploited. In this study, all the computations will be performed on the three bands but band B3 will be discarded when using the actual satellite observations.

[11] The volume of IASI data is so large that the size of the satellite data sets is a limiting factor. In this study, a set of four weeks of IASI measurements, representing a few hundred gigabytes, has been implemented: They sample the seasonal variability (the first week of January, April, July, and October 2008). Only the cloud free cases are studied here, and they are sorted using the ECMWF cloud fraction information.

### 2.2. Existing Infrared Emissivity Data Sets

#### 2.2.1. MODIS Retrieved Emissivities

[12] This study uses the MODIS MYD11 product [*Wan and Li*, 1997]. It consists of monthly mean MODIS retrievals of surface emissivity at 833.3, 909.1, 1162.8, 2500, 2564 and 2631.6 $cm^{-1}$. The retrieval is based on a day/night measurement difference algorithm. There are twelve equations: The radiative transfer equation for the six wavelengths for the day and for the night. There are fourteen unknowns: The two surface temperatures and the six emissivities for the day and for the night. Considering the daily variability of the emissivity negligible (daytime and nighttime emissivities are considered to be equal) leaves twelve equations with eight unknowns. The retrieval can only be estimated under clear conditions, due to the opacity of clouds in the infrared. Monthly mean compositing is performed, at a $0.05° \times 0.05°$ spatial resolution, to provide a full map of the emissivity. However, cloud cover can be very persistent at some locations, and the monthly mean emissivity product can still be spatially incomplete.

[13] The annual variability of this emissivity database has been analyzed. The emissivity of vegetated surfaces shows more changes than deserts, as expected, but with limited temporal variability. The highest temporal variations are observed in semi-arid transition zones, such as the sub-Sahelian region, that are very arid part of the year and covered with vegetation during the wet season. To be consistent with *Seemann et al.* [2008] work, the "4.1 collection" of the twelve months of 2007 is used.

#### 2.2.2. MODIS UCSB Emissivity Library

[14] This data set contains laboratory measurements of emissivities for different materials and soils, collected by Zhengming Wan at the Institute for Computational Earth System Science at the University of California, Santa Barbara (UCSB; http://www.icess.ucsb.edu/modis/EMIS/htm-l/em.html). The emissivity of flat materials is determined by the measure of their reflection using a Transformed Infrared (TIR) spectrometer combined with an integration sphere. This measure of their reflectance is converted into directional hemispherical emissivity using Kirchoff's law: $\epsilon = 1 - R$. This is a unique data set, but natural surfaces are usually more complex than the considered materials. For instance, their surface roughness or the inclusion/mixture of different materials will modulate the emissivity.

#### 2.2.3. ASTER Emissivity Library

[15] This data set combines different lab emissivity measurements made by the Jet Propulsion Laboratory, John Hopkins University, and the U.S. Geological Survey (http://speclib.jpl.nasa.gov/). Different spectra are available, for rocks under different states (solid, powder, sands) or vegetation types [*Salisbury et al.*, 1994]. This database supplements the MODIS UCSB measurements data set. Silicate spectra from this database are of particular importance as the MODIS UCSB emissivity library only contains a limited sample of them.

#### 2.2.4. UWIREMIS

[16] MODIS measurements (section 2.2.1) provide six surface emissivities globally at $0.05° \times 0.05°$ spatial resolution. Using these emissivities, *Seemann et al.* [2008] compute a global emissivity spectrum at ten different wave numbers (699.3, 826.5, 925.9, 1075.3, 1204.8, 1315.8, 1724.1, 2000, 2325.6 and 2777.8 $cm^{-1}$). To compute this spectrum, they use the MODIS-UCSB laboratory spectra considering a global shape: A slow decrease starting at 714.3 $cm^{-1}$ until an emissivity minimum around the absorption band of the quartz at 1162.8 $cm^{-1}$, quickly increasing at the start of the absorption band of the water vapor and then slowly decreasing and finally a highly decreasing part between 2000 and 2500 $cm^{-1}$. According to *Seemann et al.* [2008] notation, this data set will be referred to the "UWIREMIS data set."

#### 2.2.5. IASI Emissivities From NASA

[17] *Zhou et al.* [2011] retrieved infrared emissivity spectra directly from IASI measurements. First, a learning data set of atmospheric profiles is built: Each of the situations is associated to random surface skin temperatures and a random emissivity spectrum coming from the UWIREMIS data set and corresponding surface type. Radiative transfer calculations are performed on these situations to obtain associated brightness temperatures. Under some hypothesis, the radiative transfer equation is simplified into a linear model and a regression algorithm is then defined. This algorithm operates under three different conditions: Clear, cloudy, and mixed. The advantage of this algorithm is its speed, compared to more physical approaches. The database used in this study is a monthly mean of the clear retrievals for 2008. This data set will be called the "NASA data set."

#### 2.2.6. IASI's Emissivities From ARA

[18] This data set has been built by the Analyse du Rayonnement Atmosphérique (ARA) group from the Laboratoire de Météorologie Dynamique [*Pequignot*, 2006; *Pequignot et al.*, 2008; *Capelle et al.*, 2012]. A neural

network is developed to retrieve the surface temperature from AIRS measurements at selected wavelengths. The emissivity is determined for "window" wavelengths directly using the radiative transfer equation. To calculate all the terms of the radiative transfer equation for a given situation, a knowledge of the related atmospheric profile is compulsory. Here a pre-built database made of atmospheric profiles (TIGR) and the associated calculated brightness temperatures is used. They search for the situation of this database closest to the satellite measurement and use the associated atmospheric profile. In order to complete the whole emissivity spectrum, a recognition algorithm is made using laboratory emissivity spectra described in section 2.2.2. This data set has been built for the tropics only ($\pm 30^\circ$ latitude). These emissivities will be referred to as the "ARA data set."

### 2.3. Ancillary Data Sets

#### 2.3.1. ECMWF Analysis

[19] To represent the state of the atmosphere, the 6 hourly operational global analyses from the Integrated Forecasting System (IFS) from the ECMWF are considered [*Uppala et al.*, 2005]. They consist of more than 350 different variables describing the atmosphere, from the temperature to the cloud properties. The analysis of the first week of January, April, July and October 2008 are considered to match the satellite observations. The ECMWF analyses are available at four different hours of the day (at 6, 12, 18 and 24 o'clock GMT) and with a $1.125^\circ$ spatial resolution. A linear temporal interpolation and a bilinear spatial interpolation of the profiles are used to obtain a better match with the satellite observations. The cloud mask chosen to select clear situations is the ECMWF total cloud cover: The threshold for a situation to be clear is fixed at five percent cloud coverage.

#### 2.3.2. IGBP Surface Classification

[20] The International Geosphere Biosphere Programme–Data and Information System (IGBP-DIS) is a global collection of surface parameters derived from AVHRR measurements at a 1 km resolution. It results from a collaboration between the U.S. Geological Survey and the European Commission's Joint Research Centre. The DISCover data set [*Running et al.*, 1994] provides a classification of all the continental surfaces into seventeen land cover categories.

[21] In order to improve the seasonal variability of the land types, a monthly climatology of snow and ice is added to the IGBP surface classification.

### 2.4. LSA SAF Surface Temperature

[22] The Land Surface Analysis Satellite Applications Facility (LSA SAF) provides a land surface temperature derived from Meteosat Second Generation satellite (MSG). This retrieval is based on clear-sky measurements of the Spinning Enhanced Visible and Infrared Imager (SEVIRI) at channels IR10.8 and IR12.0 ($\mu$m). It is a generalized split-window algorithm with atmospheric parameters from a look-up table and a surface emissivity derived from the fractional vegetation cover also retrieved by the LSA SAF. These data are available from 2007 to now, with a measure every 15 min [*Trigo et al.*, 2011, 2008; *Caselles et al.*, 1997; *Wan and Dozier*, 1996]. This data set will be used to validate the retrievals of surface temperature from IASI. Thus a spatial and temporal collocation is performed with the IASI measurements described in section 2.1.

[23] This data set will be referred to as the "LSA SAF *Ts*."

### 2.5. Radiative Transfer Code

[24] In this study the Radiative transfer for TOVS (RTTOV) code will be used. RTTOV is a fast radiative transfer model originally developed at ECMWF [*Eyre*, 1991] and that is now supported by the EUMETSAT NWP-SAF (Satellite Application Facility) [*Saunders et al.*, 1999; *Matricardi et al.*, 2001]. The model allows for rapid simulations of radiances for satellite infrared and microwave radiometers given an atmospheric profile of temperature, variable gas concentrations, cloud and surface properties. Numerous platforms and sensors are supported. RTTOV-9 contains the forward, tangent linear, adjoint and full Jacobian matrices. It includes simulations for the sea surface emissivity, both in infrared and microwave. Clouds (liquid and ice) and rain can be considered.

## 3. Emissivity Interpolator

[25] In this section a spectral emissivity interpolator is developed. It uses the low spectral resolution emissivities from the six MODIS initial estimates to derive higher-resolution emissivity spectra. First, a global high-resolution emissivity data set is created, by combining laboratory measurements of emissivities, for each point and each month, with the help of the IGBP classification (section 3.1). Second, a principal component analysis (PCA) is performed on this database (section 3.2) to represent the high-resolution emissivity spectra with a limited number of spectral features. For each location and month in the year, a neural network interpolation (section 3.3) finally obtains the high-resolution emissivity spectra that fit the six initial MODIS emissivity (see interpolation part in scheme of Figure 2).

[26] This interpolator provides first guess emissivity spectra for the forthcoming surface and atmospheric retrievals. The first guesses have to be of good quality (see section 4.3) for the retrieval to converge and produce accurate results.

### 3.1. A Global High-Resolution Emissivity Data Set

[27] The objective here is to develop a preliminary global infrared emissivity database with IASI spectral resolution that represents the emissivity natural variability as well as possible. It will be used to perform the PCA analysis, as well as to train the interpolator.

[28] First, each laboratory spectrum of the UCSB MODIS data set (section 2.2.4) is associated to its corresponding IGBP surface class (section 2.3.2). Then, for each MODIS pixel in the map (section 2.2.2), the algorithm searches for the laboratory spectra with the same surface class and selects, among them, the five spectra closest to the six MODIS retrieved emissivities. To increase the variability close to the emissivity variability in the obtained data set, instead of taking only the closest spectrum, a linear combination of the five closest spectra is calculated, weighted by the distances to the six MODIS original emissivities. A high-resolution infrared emissivity database is therefore obtained. This data set is built at a monthly timescale in order to keep a seasonal variability.

[29] Four months are selected to provide the seasonal variability (January, April, July and October). For each month, there are $\sim$300,000 situations. This limitation on the

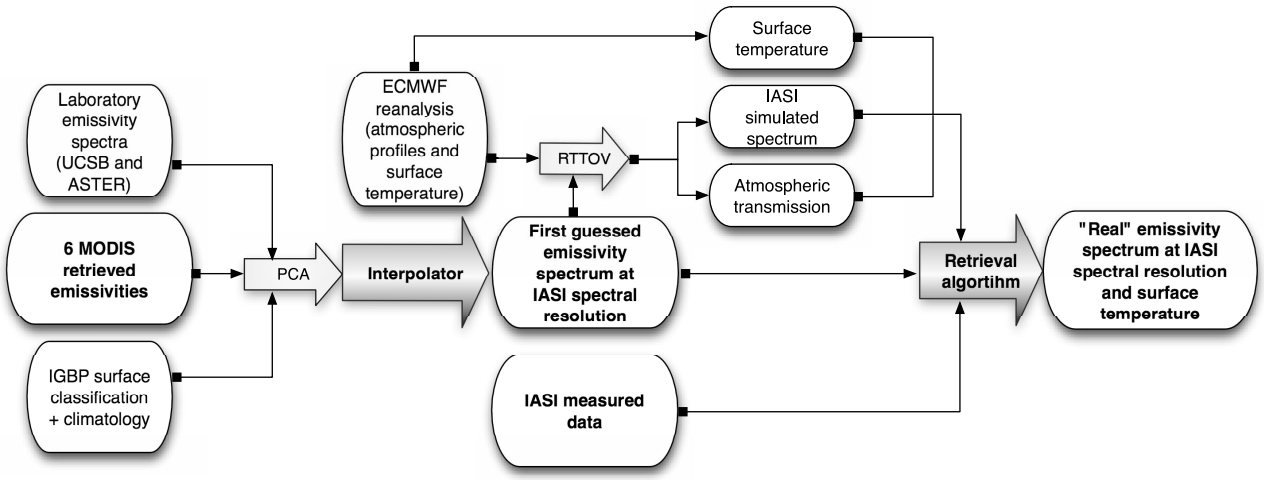


**Figure 2.** Methodology scheme for the interpolation and the retrieval algorithms.

data to be used is not a problem because of the high number of situations.

### 3.2. Principal Component Analysis

[30] Working on all IASI channels is very time-consuming and would introduce numerical difficulties. A principal component analysis (PCA) is applied on the infrared emissivity spectra. A PCA is a compression method that transforms the original variables into linear combinations of them that describe their variability with the least mean square error [*Jolliffe*, 2002].

[31] Let $\varepsilon = (\epsilon_1 \cdots \epsilon_{8461})$ be the original variables (i.e., an IASI emissivity spectrum). First, it is necessary to calculate the covariance matrix $V = \mathrm{cov}\ (\varepsilon, \varepsilon)$ of the emissivity data set of the previous section. Then, $V$ is diagonalized using a Choleski decomposition: This provides eigenvalues and their associated eigenvectors. Each eigenvector is a particular spectral feature to represent the emissivity spectra. The higher the eigenvalue is, the higher the importance of the eigenvector to explain the variability of the emissivity spectra. The eigenvalues are sorted by decreasing order so that the first eigenvectors explain the larger part of the emissivity variability:

$$(\epsilon_1 \ldots \epsilon_{8461}) = C \cdot EV + \bar{\varepsilon}$$

where $C$ is the (1 × 8461) vector representing the PCA components (i.e., new variables), $EV$ is the (8461 × 8461) eigenvector matrix, and $\bar{\varepsilon}$ is the mean emissivity spectrum.

[32] Instead of using all the 8461 eigenvectors to represent the emissivity spectra, a limited number $P$ of components is selected. In this case, $C$ has dimension (1 × $P$) and $EV$ is replaced in equation (3.2) by $EC_P$, a ($P$ × 8461) matrix. Figure 3 represents the errors induced by the reconstruction of the emissivities, with different numbers of components $P$. As expected, the spectral error decreases rapidly when increasing the number of components. Fifty components allows representing the whole emissivity data set with less than $10^{-4}$ of mean spectral error. Using ten components gives an error around $10^{-3}$, compatible with the level of accuracy required in this study. The first ten components of the PCA explain 99,89 % of the total variance of the emissivity which is satisfying.

[33] Figure 4 presents the first and fourth components as examples. Figure 4 (left) shows the eigenvector spectrum and Figure 4 (right) provides its associated geographical principal component. In order to retrieve the emissivity, each eigenvector spectrum has to be multiplied by its geographical representation and then all these products are added with the mean $\bar{\varepsilon}$ (see section 3.2). The first eigenvector (Figure 4, top) represents the largest spectral variability of the emissivities: The main shift in emissivity corresponds to the silicate absorption between 1000 and 1200 $cm^{-1}$. This corresponds to the double vibration band of the quartz. The silicate structures over the Saharan desert and Australia can be observed on the map [*Jiménez et al.*, 2010]. Vegetation and water IR spectra are very flat compared to the strong signature of the silicates.

[34] The difficulty with a PCA is that it mixes all the information in the first components so that they represent as

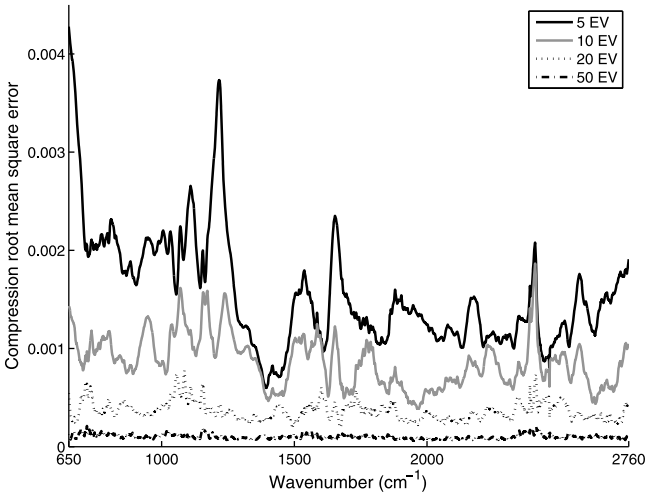


**Figure 3.** Mean emissivity spectral errors due to the principal component analysis (PCA) compression using 5, 10, 20, and 50 components, over the global database of combination of laboratory spectra built.

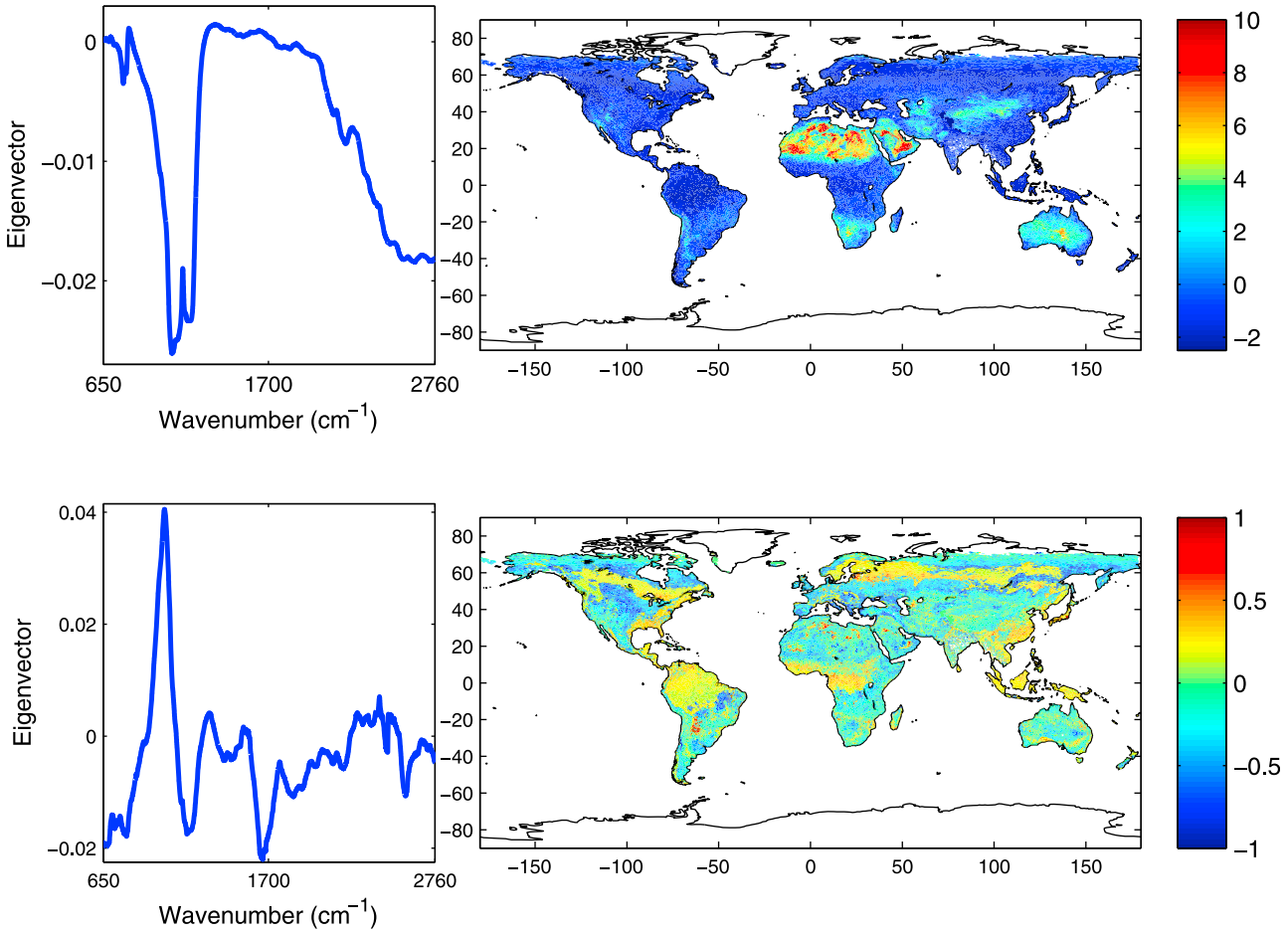


**Figure 4.** Eigenvectors of (left) the IASI emissivity spectrum and (right) their corresponding spatial location, for (top) the first and (bottom) the fourth principal components.

much variance as possible. The high-order eigenvectors contain the remaining spectral features and become difficult to interpret spatially. Furthermore, the strong silicate signature influences all the eigenvectors significantly, and there is not much spatial features outside the arid regions.

[35] The fourth eigenvector is shown in Figure 4 (bottom). It has a strong spectral anomaly around the silicate signature but it appears to be essentially related to vegetation spatial structures. As the mean spectrum includes strong signatures related to the silicates, the PCA compensates with higher order orthogonal features to obtain the quasi-flat vegetation spectrum.

### 3.3. Spectral Emissivity Interpolator

[36] The objective is to interpolate the six MODIS retrieved emissivities (section 2.2.1) in order to retrieve a high-resolution infrared emissivity spectrum represented by a fixed number of PCA components. As this problem is clearly not linear, a non-linear model is chosen here, i.e., a multilayer perceptron neural network. In *Seemann et al.* [2008], a similar strategy is developed but using a linear regression instead of a neural network.

[37] The interpolation scheme is based on a neural network (NN) [*Rumelhart et al.*, 1986] with three layers: (1) an input layer with neurons representing to the six initial MODIS emissivities; (2) a hidden layer with neurons linked to the neurons of the input layer with a special weight and giving to each of the neurons of the output layer a transformation of it; and (3) an output layer with neurons corresponding to the ten first components of the PCA (section 3.2). After trial and error tests, the use of twenty neurons in the hidden layer appears to be a good compromise.

[38] Each neuron of the hidden layer makes two operations: First, the $i$th neuron computes the weighted sum $h_i$ from its $p$ entries, $x_j$:

$$h_i = \sum_{j=1}^{p} w_{j,i} \cdot x_j$$

[39] Then, it adds to his entry $h_i$ a bias $b_i$ and applies a sigmoid function $\sigma$:

$$y_i = \sigma(h_i + b_i)$$

[40] A cost function, the mean quadratic error between the outputs of the network and the target outputs from the learning database, is minimized thanks to a back-propagation algorithm [*Rumelhart et al.*, 1986], based on a stochastic gradient descent (i.e., the Levenberg Marquardt method).

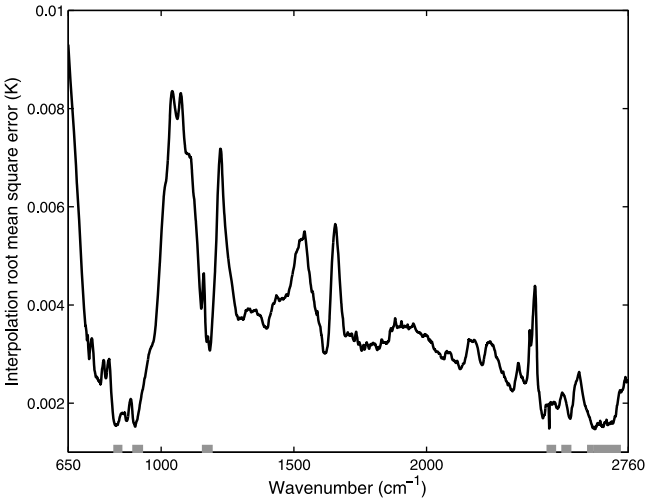


**Figure 5.** Spectral errors of the emissivity first guess interpolator calculated over the test database previously built. The location and spread of the Moderate Resolution Imaging Spectroradiometer (MODIS) channels are represented on the horizontal axis.

[41] The NN training database is composed of a large variety of MODIS emissivities (i.e., NN inputs) and their associated infrared PCA components (i.e., NN outputs). The emissivities at MODIS frequencies are extracted from the high-resolution spectral emissivity data set described in section 3.1. The initial high-resolution data set is made of four months of 300,000 situations which is too much for the learning process. 288,000 situations are randomly sampled and are divided in three parts, one for the learning (83.3%, which makes 240,000 situations randomly selected), and two other parts for the test and validation databases (8.3% for each which makes 24,000 different situations). The validation database is used to verify that there is no overfitting during the learning. The NN has not been calibrated using this validation data set so the errors are estimated on it at each step of the learning and any increase stops the learning process. The test data set is used at the end of the learning stage to evaluate the quality of the NN results.

[42] Taking into account ten PCA components for the infrared emissivities is satisfactory since it provides a compression error lower than the mean error expected from the interpolator, around $4 \times 10^{-3}$ (see Figure 5). Different numbers of PCA components have been tested for the interpolator. Using more components actually increased the interpolation errors: The NN interpolator has only six pieces of information as inputs (i.e., the six initial MODIS emissivities), and trying to retrieve many more degrees of freedom makes the interpolation unstable.

### 3.4. Errors Estimates

[43] To measure the quality of the infrared emissivity interpolator, some statistics are performed on the test database defined in the previous section.

[44] Figure 5 represents the spatial mean of the root mean square (RMS) error of the interpolator, calculated on a test database extracted from the database build in section 3.1, not used for the learning of the interpolator. First, this plot shows that the interpolation error is higher than the PCA compression errors when using ten components. This validates our choice of using ten PCA components. On the horizontal axis of Figure 5, the six wavelengths retrieved from MODIS are represented with their spectral width, in grey. The error is relatively low, even in the 1300–2500 cm$^{-1}$ domain where there is no MODIS information but as expected the errors are lower at the MODIS wavelengths. Overall, the infrared spectral interpolator manages to retrieve the spectrum very satisfactorily: The mean spatial and spectral error is $3.5 \times 10^{-3}$.

[45] The mean spectral interpolation RMS error is shown in Figure 6 for July 2008. As expected, the locations associated with the higher spectral variations (desert areas with silicates) are also the locations where the errors of the interpolator are higher. However, the errors remain low compared to the emissivity values even at these locations (around 1%). The spatial distribution of the interpolation error statistics confirms that the PCA components over arid regions are, as expected, the most important, as those places have the higher spectral variations.

[46] As an example, Figure 7 presents the interpolation of a spectrum over the Sahara desert. The black line corresponds to the original spectrum from the high-resolution emissivity database, the horizontal black lines correspond to the inputs to the interpolator (i.e., the six initial MODIS emissivities), and the grey line represents the interpolated spectrum. Here, it can clearly be seen that even in the domain where the interpolator has no information from MODIS inputs, the use of the PCA components allows providing reasonable spectral features and obtaining a realistic emissivity spectrum, as the two grey curves are very close to each other.

## 4. Simultaneous Retrieval of Surface Temperature and Emissivity

[47] The use of a climatological emissivity first guess is sometimes sufficient for some applications. However, it is possible to refine this first guess by using a retrieval scheme and real time observations. In this section, a physical inversion scheme is developed to retrieve simultaneously the emissivities and the surface temperature.

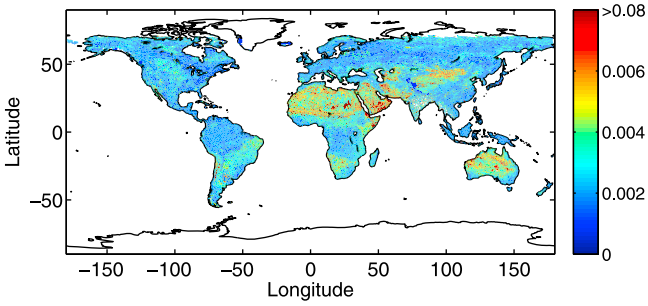


**Figure 6.** Map of the root mean square (RMS) errors of the emissivity first guess interpolator, averaged over the full IASI spectrum, calculated on the database previously built corresponding to the month of July.

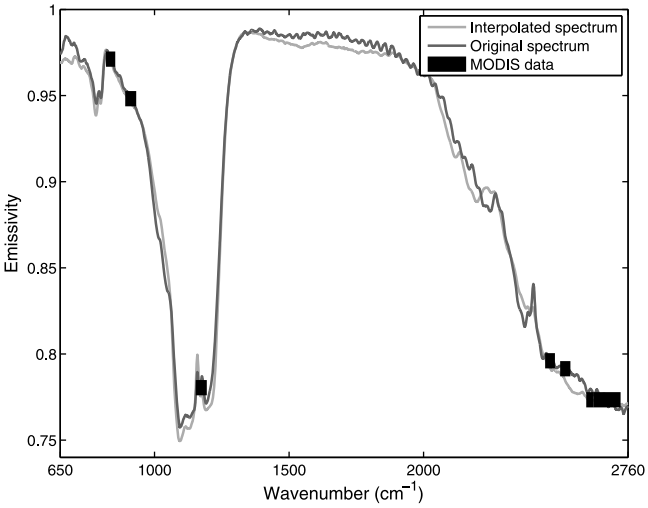


**Figure 7.** An example of a spectral interpolation of a typical arid soil emissivity spectrum. The original spectrum is darker gray, the interpolation is lighter gray. The location, spread, and value of the MODIS channel interpolation (inputs) are also represented.

### 4.1. Method

[48] The radiance $I_{obs}$ measured by the IASI instrument at wavelength $\lambda$ is given by the radiative transfer equation:

$$I_{obs}(\lambda) = \tau(\lambda) \cdot \epsilon_{true}(\lambda) \cdot B(T_{s_{true}})(\lambda) + atm_{true}\uparrow(\lambda) \cdot (+\tau(\lambda) \cdot (1 - \epsilon_{true}(\lambda)) \cdot atm_{true}\downarrow(\lambda)) \quad (1)$$

with $\tau(\lambda)$ the atmospheric transmission at $\lambda$, $atm_{true}\uparrow$ the atmospheric up-welling contribution, $atm_{true}\downarrow$ the atmospheric down-welling contribution, $\epsilon_{true}$ the emissivity of the surface, and $T_{s_{true}}$ its temperature. All the variables are here named *true* in order to differentiate them from their following estimations.

[49] Using a first guess, *fg*, for surface and atmospheric variables coming from the ECMWF analyses, RTTOV simulations estimate the radiance $I_{calc}$ that would be observed by IASI at wavelength $\lambda$ under these conditions. The formulation is the same as equation (1) but with *fg* instead of *true*.

[50] Let us consider these equations at $N$ wavelengths where the atmosphere is transparent, $\lambda_1 \ldots \lambda_N$ (these wavelengths will be selected later), i.e., where the atmospheric terms are neglected compared to the surface terms. In these cases, the first guesses and the true atmospheric contributions can be considered as approximatively equal, which implies:

$$(I_{obs} - I_{calc})(\lambda) = \tau(\lambda) \cdot \left(\epsilon_{true}(\lambda) \cdot B(T_{s_{true}})(\lambda) - \epsilon_{fg}(\lambda) \cdot B\left(T_{s_{fg}}\right)(\lambda)\right)$$

This can be written as

$$\epsilon_{true}(\lambda) \cdot B(T_{s_{true}})(\lambda) = \underbrace{\left(\frac{I_{obs} - I_{calc}(\lambda)}{\tau(\lambda)}\right) + \epsilon_{fg}(\lambda) \cdot B\left(T_{s_{fg}}\right)(\lambda)}_{A} \quad (2)$$

[51] Using the PCA notation defined in section 3.2, the emissivity can be approximated by

$$\epsilon \approx (c_1 \ \cdots \ c_P) \cdot EV_{P,N} + \bar{\epsilon} \quad (3)$$

where $P$ is the number of components being used, $\bar{\epsilon}$ is the mean emissivity spectrum, and $EV$ part of the eigenvector matrix defined as:

$$EV_{P,N} = \begin{pmatrix} ev_{1,1} & \cdots & ev_{1,N} \\ \vdots & \ddots & \vdots \\ ev_{P,1} & \cdots & ev_{P,N} \end{pmatrix}$$

[52] Merging with equation (2) yields

$$C \cdot EV_{P,N} + \underbrace{\frac{-A}{B(T_{s_{true}})}}_{F\left(T_{s_{true}}\right)} = -\bar{\epsilon} \quad (4)$$

[53] The function $F$ depends upon the wavelength $\lambda$. For a given wavelength $\lambda_i$, $F_i$ is defined as

$$F_i(T_{s_{true}}) = -A_i \cdot \frac{\lambda_i^5}{2 \cdot h \cdot c^2} \cdot \left(e^{\frac{h \cdot c}{\lambda_i \cdot k \cdot T_{s_{true}}}} + 1\right)$$

[54] This equation is simplified by replacing $F$ by its first degree Taylor expansion around the first guess. This linear approximation is acceptable if the first guess is good enough. The retrieval will not be very different from the first guess and the first degree Taylor expansion is a good local approximation to the Plank function:

$$F_i'(T_{s_{true}}) = A_i \cdot \frac{\lambda_i^5}{2 \cdot h \cdot c^2} \cdot \frac{h \cdot c}{\lambda_i \cdot k \cdot T_{s_{true}}^2} \cdot e^{\frac{h \cdot c}{\lambda_i \cdot k \cdot T_{s_{true}}}}$$

[55] So $F_i$ is approximated by

$$F_i(T_{s_{true}}) \approx F_i\left(T_{s_{fg}}\right) + F_i'\left(T_{s_{fg}}\right) \cdot \underbrace{\left(T_{s_{true}} - T_{s_{fg}}\right)}_{\Delta T}$$

[56] Getting back into equation (4) gives

$$(c_1 \cdots c_P \Delta T) \cdot \underbrace{\begin{pmatrix} ev_{1,1} & \cdots & ev_{1,N} \\ \vdots & \ddots & \vdots \\ ev_{P,1} & \cdots & ev_{P,N} \\ F_1'\left(T_{s_{fg}}\right) & \cdots & F_N'\left(T_{s_{fg}}\right) \end{pmatrix}}_{M} = -\bar{\epsilon} - F\left(T_{s_{fg}}\right)$$

Each side of this equation can be right-multiplied by the pseudo-inverse of $M$, so that

$$(c_1 \ \cdots \ c_P \Delta T) = \left(-\bar{\epsilon} - F\left(T_{s_{fg}}\right)\right) \cdot M^T \cdot \left(M \cdot M^T\right)^{-1} \quad (5)$$

[57] With this physical inversion method, the emissivity components, $(c_1 \ \cdots \ c_P)$, and the surface temperature, $T_{s_{true}} = T_{s_{fg}} + \Delta T$, can be estimated, knowing the radiances measured by the satellite, a good first guess for the surface

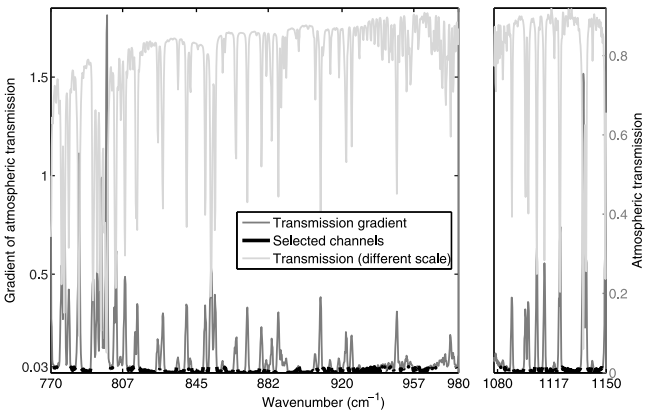


**Figure 8.** Gradient of the atmospheric transmission (darker gray). Channels with a gradient lower than 0.03 are selected for the retrieval and are indicated in black. The atmospheric transmission is also represented in lighter gray on a different scale.

and atmospheric variables, and the radiative transfer simulated radiances.

### 4.2. Selection of *N* and *P*

[58] Two parameters need to be defined in the preceding inversion scheme: *N*, the wavelengths used in the retrieval scheme, and *P*, the number of PCA components that are considered in equation (3).

[59] The selection of $\lambda_1 \ldots \lambda_N$, the window wavelengths used in the retrieval algorithm, is critical: The retrieval algorithm is based on the assumption that the first guess atmospheric contribution is equal to the real one. If only "window" channels are considered, the atmospheric contribution will be low compared to the surface one and the former assumption will be closer to reality. Among the three window domains in IASI spectra (770–980 cm$^{-1}$, 1080–1150 cm$^{-1}$ and 2420–2700 cm$^{-1}$) only the first two are considered here since the third one is too much contaminated by instrumental noise (i.e., very low signal-to-noise ratio and solar contamination). The atmospheric transmittance is calculated for each situation using the corresponding ECMWF analysis and RTTOV model, and the gradient of the atmospheric transmittance with respect to the wavelength is computed (Figure 8). Selecting the channels with low atmospheric transmission gradient ensures that they are not perturbed by any atmospheric absorption line. A threshold needs to be defined and a compromise has to be made: A low threshold would imply that the selected channels are very transparent, whereas a higher threshold will mean that more channels are kept and the inverse problem is better constrained. A threshold of 0.03 is selected after a few tests and an analysis of its impact on the retrieval algorithm statistics. This resulted in the selection of $N = 512$ channels for the retrieval scheme.

[60] To choose the number of PCA components, *P*, multiple tests have been performed. Selecting too many PCA components increases the number of degrees of freedom to characterize and the inversion problem becomes unstable. If the system is too little constrained, it can result in unrealistic solutions (e.g., emissivities too low or surface temperatures higher than 350 K). A posteriori retrieval test has been defined to detect these unstable cases: If the shift in surface temperature is more than 20 K, the retrieval is considered unstable. These unstable situations are filtered out. Figure 9 illustrates the selection of the number *P*. In Figure 9 (top) , the mean RMS error between observed and simulated BT (brightness temperatures), ($BT_{obs} - BT_{sim}$), is plotted as a function of the number of components *P*. The error decreases until *P* equals ~15, and then increases. In Figure 9 (bottom) the percentage of situations where the algorithm retrieved stable results (as defined before) is also plotted as a function of *P*. Using more than10 components makes this percentage decrease very fast, confirming that too many components impair the retrieval. The higher the number of components used is, the bigger the domain of the solution is. Thus, with more components, the problem becomes underconstrained and the pseudo-inversion is not precise enough.

[61] The ($BT_{obs} - BT_{sim}$) RMS error of the upper part first decreases because of the better representation of the spectra by the retrieved components, but this decrease continues further because there are fewer situations retrieved and included in the statistics. As a consequence, selecting ten components appears to be a good compromise.

[62] It is noticeable that even when taking only a few PCA components, unstable situations are still present. The quality of the cloud flag can significantly impact the retrieval accuracy. The ECMWF total cloud cover mask is not perfect, and cloudy situations might be missed. In these cases, the radiative transfer calculations will be mistakenly performed without taking cloud interactions into account, resulting in large differences with the observations. The retrieval scheme might try to correct the surface characteristics artificially to obtain a simulated radiance spectrum close to the measured one. This fact confirms the choice of filtering the unstable situations. This a posteriori test allows the retrieveal not to suffer from the quality of the ECMWF cloud flag.

[63] In summary, the algorithm solves a system with 512 observations and eleven unknowns (i.e., the ten emissivity PCA components plus the surface temperature shift). The inverse problem is over-constrained, which is positive: Redundancy in observations reduces the sensitivity of the retrieval to noise.

### 4.3. Sensitivity of the Retrieval to the Emissivity First Guess

[64] To test the sensitivity of the retrieval to the quality of the emissivity first guess, a series of tests are conducted.

[65] First, using constant 0.98 emissivity as first guess (for all location and wavelength), the retrieval is unstable: The retrieved surface temperature is very high and the retrieved emissivities are unrealistic. This can be explained by the use of the PCA in the retrieval scheme: The PCA cannot easily represent constant emissivity spectra as such spectra were not included in the database built in section 3.1 and used to define the PCA (section 3.2). This means that the first guess emissivity PCA components are far from realistic. As a consequence, the linearization of the radiative transfer in the retrieval algorithm becomes crude and the inversion unstable. This first experiment shows that a good first guess, compatible with the PCA used in the retrieval algorithm, is necessary. This also justifies the development of a spectral

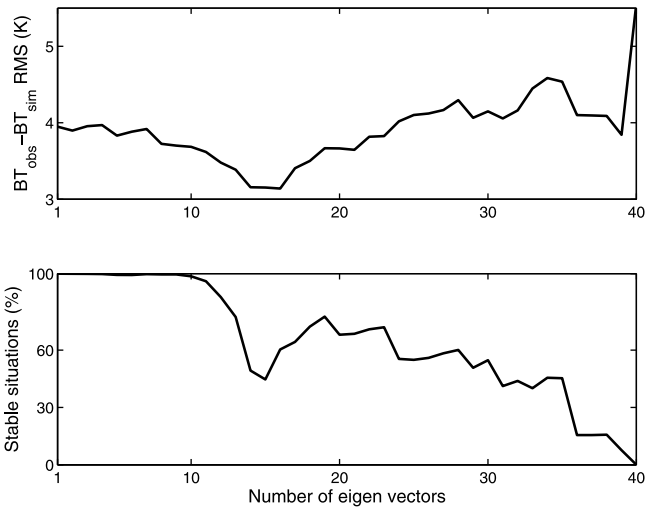


**Figure 9.** Number of emissivity PCA components used in the retrieval. (top) Mean ($BT_{obs} - BT_{sim}$) RMS error as a function of the number of components. (bottom) Percentage of retrieved stable situations as a function of the number of components.

emissivity interpolator, coherent with our retrieval scheme, using pre-existing emissivity data sets.

[66] A second series of tests is conducted to check the stability and speed of the retrieval algorithm. Since the inversion uses a first guess and then improves it, it is possible to iterate the algorithm multiple times and check the convergence of the solution. These tests (not shown) indicate that with a quality emissivity first guess, the retrieval algorithm converges in one iteration only, making it unnecessary to perform multiple iterations. This shows that our algorithm provides, rapidly, robust solutions.

## 5. Retrieval Results and Evaluation

### 5.1. Experimental Conditions

[67] Since the number of in situ measurements of emissivity and surface temperature over the globe is limited in space and time, it is difficult to use them for the retrieval validation. As a consequence, alternative strategies have been developed in order to compensate for the lack or the difficulty of use of the in situ data. *Zhou et al.* [2011] or *Hulley et al.* [2009] compare emissivity retrievals to laboratory measurements but this method is restricted to homogeneous surfaces (these studies focused on the Namib and Kalahari deserts) in order to limit the inherent different spatial resolutions between a satellite retrieval and an in situ point measurement.

[68] In *Li et al.* [2010], a sophisticated method is developed to assess the quality of emissivity retrievals. Radiative transfer simulations using the surface temperature and emissivities are compared to observed radiances, but differences between channels are considered rather than the channels themselves. This method allows theoretically to get rid of the other sources of error such as atmospheric profiles or land surface temperature. It is not implemented here because the objective is to validate not only the retrieved emissivity spectrum but also the retrieved *Ts.* Moreover, keeping the errors on the atmospheric profiles in the calculation of the difference of simulated and observed brightness temperatures allows verifying that the algorithm is not compensating those atmospheric errors by modifying its retrieval. Indeed, as all the radiative transfer calculations will use the same atmospheric profiles from the ECMWF analyses, the same features (due to bad atmospheric characterizations) should be observed on the spectra.

[69] In this paper, the *Ts* and surface emissivities retrieved from IASI measurements using MODIS retrievals as first guess, are used as inputs to a radiative transfer model and the simulations, $BT_{sim}$, are compared to the actual IASI measurements, $BT_{obs}$. Like in *Vogel et al.* [2011], this direct comparison with real satellite measurements is preferred for its simplicity and direct interpretability. The ($BT_{obs} - BT_{sim}$) statistics can directly be used to measure the spectral and spatial impacts of the retrieved *Ts* and emissivity on the radiative transfer simulations.

[70] The data set used in this section is composed of the four weeks of IASI real observations in 2008 (section 2.1). The corresponding surface characterization, atmospheric profile and cloud flag from the ECMWF analysis are collocated with each IASI measurement. To evaluate the different sources of emissivity information, the comparison is performed using several emissivity sources: (1) the various first guess data sets described in section 2.2: UWIREMIS that is anchored to MODIS, ARA that uses AIRS observations, and NASA that are IASI retrievals; (2) the first guess emissivity from our interpolation scheme, called "interpolated," anchored to MODIS (section 3); and (3) the retrieved emissivities, called "retrieved," that are based on IASI observations (section 4).

[71] The first guess emissivities are calculated for 2007, and applied to the retrieval of IASI observations from 2008 in order to test their value as first guesses. However, note that the NASA emissivity first guess is available for 2008 only. This should provide an advantage to this database. Note that all the simulations are performed for the same global data set composed of the four weeks of real IASI observations in 2008, except for the radiative transfer simulations with ARA emissivities that are restricted to the tropical belt ($\pm 30^\circ$ in latitude).

### 5.2. Spectral Analysis

[72] Figure 10 shows the spectral ($BT_{obs} - BT_{sim}$) RMS errors resulting from the use of the different emissivity databases. The dark blue curve corresponds to the ($BT_{obs} - BT_{sim}$) RMS error when using the ARA emissivities, the ECMWF *Ts*(used as first guess in the retrieval algorithm) and the ECMWF analyses as entries for RTTOV simulations. The green curve is the same but using the UWIREMIS emissivities, the red one uses the NASA emissivities and the light blue one uses the first guess interpolated emissivities. The dark curve corresponds to the ($BT_{obs} - BT_{sim}$) RMS error using the retrieved emissivities and the retrieved *Ts* as inputs to RTTOV, whereas all the other curves are using the ECMWF *Ts.* Some curves are not visible because they are very close to the light blue one.

[73] Only the IASI bands B1 and B2, from 645 to 2000 $cm^{-1}$, are presented here because band B3 has too much contamination from instrument noise and solar contamination (see section 2.1). Few channels between 660 and

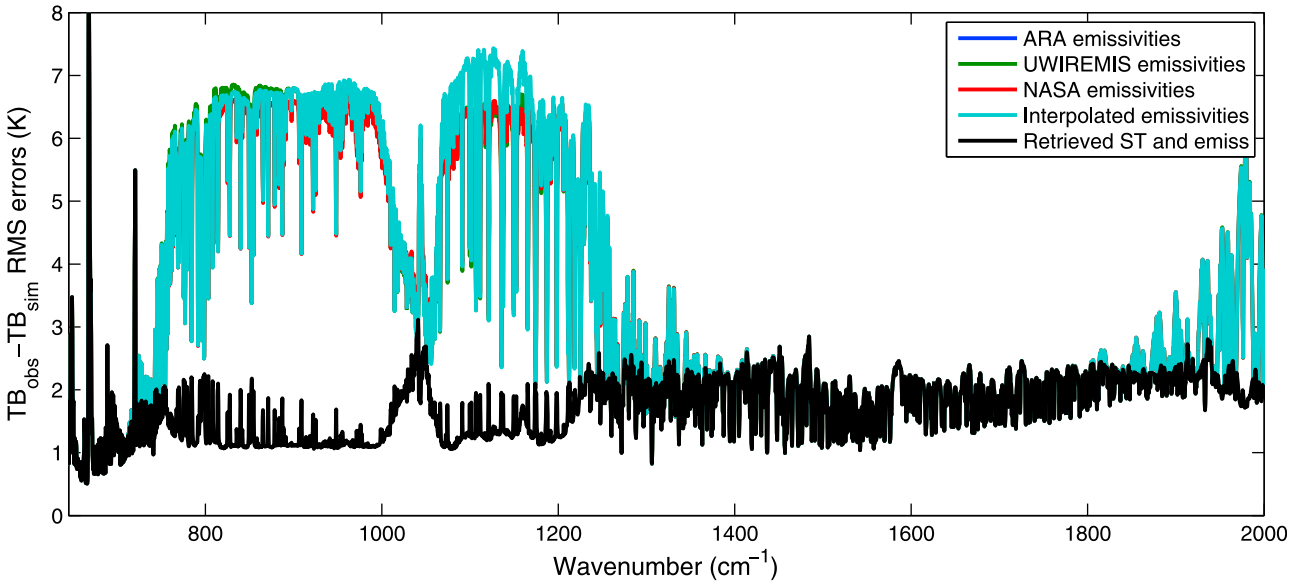


**Figure 10.** Spectral ($BT_{obs} - BT_{sim}$) RMS errors when using first guess emissivities from ARA, UWIREMIS, NASA, and interpolated emissivities and when using the retrieved surface temperature and emissivities. These statistics are a mean calculation for a set of IASI data made of the first week of January, April, July, and October.

700 $cm^{-1}$ have high ($BT_{obs} - BT_{sim}$) RMS error values, regardless of the emissivity database. These errors result from minor absorption lines not taken into account in the radiative transfer simulations. Since they do not involve surface properties, these particular channel statistics will not be discussed further.

[74] The ozone absorption band is clearly visible between 1000 and 1100 $cm^{-1}$ on all the simulations: Regardless of the surface estimates, the radiative transfer simulations are very close in this spectral domain as the error is dominated by uncertainties in the ozone concentration, not in the surface characteristics. This is a positive point: The retrieval algorithm does not artificially compensate for atmospheric profile errors by mistakenly modifying the surface parameters.

[75] The largest differences between the ($BT_{obs} - BT_{sim}$) RMS errors using the various emissivity sources are located, as expected, in the "window" spectral regions where the surface plays the dominant role. Since only *Ts* and emissivities are changed in the radiative transfer simulations, there should be no difference in the spectral regions mainly sensitive to the atmosphere.

[76] First, the simulations using different sources of emissivities and the first guessed *Ts* are compared (the colored curves, not considering the black one). The NASA emissivities perform slightly better than the other databases. This is not surprising: First, they are calculated for 2008, not for 2007 as for the other emissivities. Second, they are directly estimated from IASI observations, contrarily to the other emissivity databases that are anchored to the six MODIS emissivities (section 3). The results from our interpolator and from the UWIREMIS data are very close, except in the 1100–1200 $cm^{-1}$ silicate absorption band. This can be explained by the fact that *Seemann et al.* [2008] added a priori information about the spectral shape of the emissivities in this region, not included in our interpolation scheme. Yet, rather similar results are obtained when changing only the monthly estimates of the emissivity in the calculation (the colored curves), those different data sets are equivalent.

[77] The impact is much more significative when both the retrieved emissivities and surface temperatures are used (black line). For this configuration, the error decreases to less than 2 K in the "window" regions, nearly 4 K lower than the statistics obtained with only the emissivity first guesses. The spectral mean of the ($BT_{obs} - BT_{sim}$) RMS error when using ARA, NASA, UWIREMIS or the interpolated emissivities is around 3.5 K but it reduces to 1.7 K when using both the retrieved surface temperature and emissivities. A similar result can be observed concerning the standard deviation of the ($BT_{obs} - BT_{sim}$) RMS error that decreases from around 2 K to 0.5 K. These results demonstrate that the new physical retrieval scheme is able to considerably improve the surface contribution in the radiative transfer simulations.

[78] The RMS error decreases when using the retrieved emissivity and temperature is obviously due, for a large part, to the better estimate of the surface temperature. As noted in *Vogel et al.* [2011], it is difficult to measure the impact of a better emissivity when the surface temperature is very inaccurate. Thus, a second radiative transfer calculation comparison is performed. Different emissivities are combined with the retrieved surface temperature, the atmospheric parameters remaining the same. The ($BT_{obs} - BT_{sim}$) RMS errors are shown on Figure 11, for a constant emissivity of 0.98 (light grey curve), for the interpolated first guessed emissivity (dark grey), and for the retrieved emissivities (black curve). The calculations using NASA, ARA or UWIREMIS emissivities are not shown as they are very close to the results using the interpolated emissivity. This figure clearly shows that with a better *Ts*, the impact of a good emissivity is more visible. First, comparison of the results

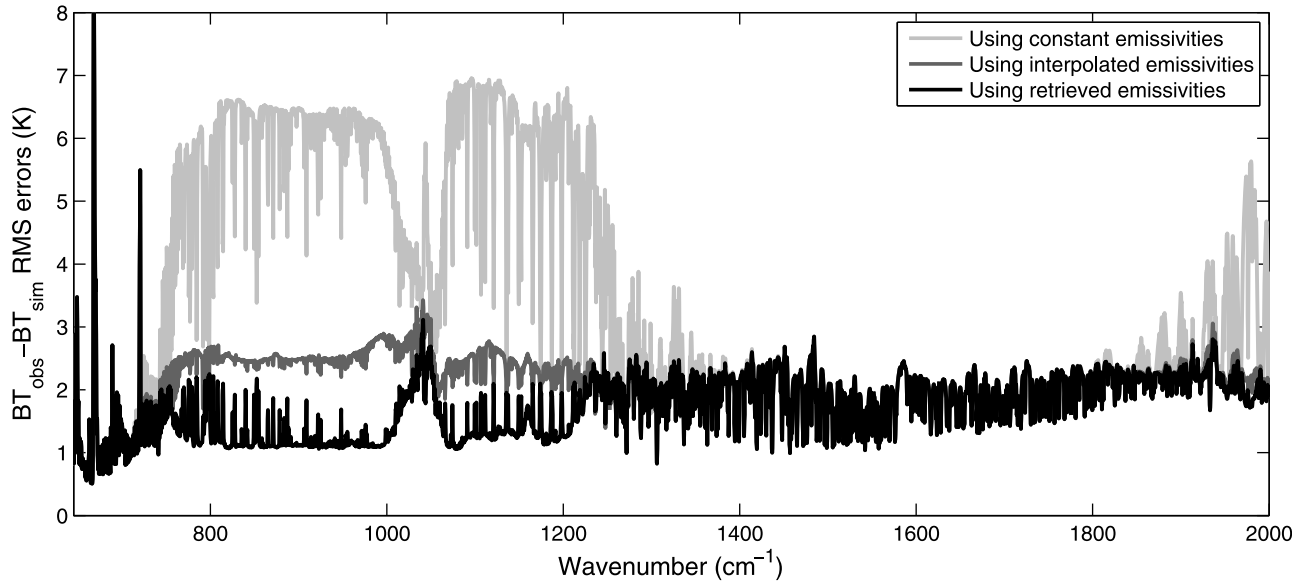


**Figure 11.** Spectral ($BT_{obs} - BT_{sim}$) RMS errors when using retrieved surface temperature plus constant (lighter grey), interpolated (darker grey), and retrieved (black) emissivities. These statistics are a mean calculation for a set of IASI data made of the first week of January, April, July, and October.

with a constant emissivity and with the interpolated first guessed emissivity shows the benefit of taking into account the spectral dependence of the emissivities, thus justifying the interpolation tool. Second, the retrieval scheme significantly improves the first guessed emissivities. The interpolated emissivities are a monthly mean first guess whereas the retrieved ones are daily estimates that can account for daily variation of surface characteristics such as soil moisture variation. *Mira et al.* [2007] showed that these variations could lead to emissivity differences around 15%. The remaining RMS errors on Figure 11 are similar in the "window" regions and in the atmospheric sounding spectral domains. Therefore, the surface retrievals can be considered to be well characterized. This figure confirms also that a precise surface characteristics knowledge is very important in order to determine the state of the atmosphere. Indeed, the remaining differences between the radiative transfer simulations and measured observations are the result of inaccurate atmospheric information, radiative transfer errors or bad calibration. These differences can be exploited by a retrieval scheme to estimate the atmospheric variables without being contaminated by the surface. This will be further discussed in the conclusion.

### 5.3. Evaluation of the Retrieved *Ts*

[79] In order to analyze the spatial structure of the retrieval and quantify the committed error, the retrieved *Ts* are compared to *Ts* derived from SEVIRI, provided by LSA SAF (section 2.4). This comparison is very interesting because these two *Ts* data sets have been built using different instruments and methods. Thus the errors in the different data sets should not be correlated.

[80] As LSA SAF *Ts* comes from SEVIRI on board MSG, these *Ts* are only available on a disk centered over Northern Africa. In order to have a spatial coherence, the LSA SAF *Ts* are spatially collocated with the retrieved ones. LSA SAF *Ts* is available every fifteen minutes, so the temporal collocation is very accurate with the *Ts* retrieved from IASI measurements.

[81] The overall RMS error, bias and standard deviation between the two data sets are computed. A similar comparison is performed between the *Ts* provided by the ECMWF (used as first guess in the retrieval scheme) and the LSA SAF *Ts.* The results are shown in Table 1. The comparison between the retrieved *Ts* and the LSA SAF *Ts* shows a lower bias and standard deviation (respectively by 62% and 49%) and thus a lower RMS error (by 52%) than when compared with the ECMWF *Ts.* This means that the retrieved and LSA SAF *Ts* data sets are more coherent.

[82] Figure 12 shows the difference between (1) the retrieved *Ts* (Figure 12, top) and (2) the ECMWF *Ts* (Figure 12, bottom), and the LSA SAF ones. The data of the full data set (first week of January, April, July and October) are composited in this figure to obtain a more complete map (individual months have been compared and show similar features). This map shows a clear negative bias of the ECMWF *Ts* with respect to the LSA SAF *Ts.* Some spatial features are noticeable on the difference between ECMWF and LSA SAF *Ts* map and disappear on the comparison with the retrieved *Ts.* For example, there is a positive bias on the northern Europe between ECMWF and LSA SAF *Ts* that does not appear on the retrieved map. All over the Saharan desert, the differences are higher (in absolute value) between ECMWF and LSA SAF *Ts* than when comparing with the retrieved *Ts.* At the edge of the satellite disk, particularly in the Arabian Peninsula, large errors can be observed. They can be due to LSA SAF *Ts* inaccuracy at high scanning angles, especially in the Arabian Peninsula where an error on the LSA SAF *Ts* higher than 3 K is expected [*Freitas et al.*, 2010].

[83] No spatial error structure can be clearly identified for the retrieved *Ts*, this tends to show that the quality of the emissivity retrieval does not depend upon surface types nor geological structures.

**Table 1.** Comparison Between Land Surface Analysis Satellite Applications Facility (LSA SAF) *Ts* and the European Centre for Medium-Range Weather Forecasts (ECMWF) *Ts* or the Retrieved *Ts*

| Database | RMS (K) | Bias (K) | Standard Deviation (K) |
|---|---|---|---|
| ECMWF LSA SAF *Ts* | 8.7 | −6.0 | 6.3 |
| Retrieved LSA SAF *Ts* | 4.2 | 2.3 | 3.5 |

[84] The LSA SAF *Ts* and the retrieved ones have been computed using different methods and measurements. The fact that the two databases are in a good agreement tends to give confidence to the two data sets.

[85] Another method to compare the three databases (ECMWF, LSA SAF, and retrieved surface temperature) is the triple collocation technique [*Janssen et al.*, 2007; *Stoffelen*, 1998]. Let $X$, $Y$ and $Z$ be the three surface temperature estimates. The triple location method is based on the hypothesis that these estimates are an addition of the true surface temperature, *Ts*, and an error term:

$$X = Ts + \epsilon_X$$
$$Y = Ts + \epsilon_Y$$
$$Z = Ts + \epsilon_Z$$

where $\epsilon_X$, $\epsilon_Y$ and $\epsilon_Z$ are the errors on *Ts* for $X$, $Y$ and $Z$. These errors are supposed to be uncorrelated. It is also assumed that the three estimations are unbiased, if this is not the case, the average value of $X$, $Y$ and $Z$ can always be suppressed. In this case, the retrieved *Ts* have been lowered by 2.3 K and the ECMWF *TS* have been increased by 6.0 K (only in the triple correlation calculation) to match with the mean LSA SAF *Ts*.

[86] From these hypotheses, it can be shown that

$$\overline{(X-Y)\cdot(X-Z)} = \overline{\epsilon_X^2} \quad (6)$$

$$\overline{(Y-X)\cdot(Y-Z)} = \overline{\epsilon_Y^2} \quad (7)$$

$$\overline{(Z-Y)\cdot(Z-Y)} = \overline{\epsilon_Z^2} \quad (8)$$

where the horizontal bar represents the statistical expectation. Indeed, all the terms mixing two estimations are equal to zero ($\overline{\epsilon_X\epsilon_Y} = 0$, $\overline{\epsilon_X\epsilon_Z} = 0$, $\overline{\epsilon_Y\epsilon_Z} = 0$) since they are uncorrelated.

[87] The complete triple collocation algorithm also considers a scaling factor for $Y$ and $Z$, such as $Y = \beta_Y \times Ts + \epsilon_Y$. Then, using a neutral regression those two scaling factors can be determined [*Marsden*, 1999]. Here, the scaling factors obtained are so close to unity that this method is not presented. Yet, it shows that the three *Ts* databases are very consistent.

[88] By solving the system presented in equation (8), the results obtained correspond to an uncertainty estimate of 5.4 K for the ECMWF *Ts*, 3.1 K for the LSA SAF, and 1.5 K for the retrieved *Ts*. These results can be explained by the fact that the two satellite retrievals are in better agreement, and the triple location gives more confidence in their estimation. The fact that the retrieved *Ts* obtains the lower error score can also be related to the fact that it is closer to ECMWF estimations than the LSA SAF *Ts*. This can be shown by looking at the correlation coefficients:

$$Cor(\text{ECMWF}, \text{LSA SAF}) = 0.78$$
$$Cor(\text{ECMWF}, \text{Retrieved}) = 0.83$$
$$Cor(\text{Retrieved}, \text{LSA SAF}) = 0.94$$

[89] The LSA SAF *Ts* are more correlated with the retrieved *Ts* than with the ECMWF *Ts*, on the other hand, the ECMWF *Ts* are more correlated with the retrieved *Ts* than with the LSA SAF *Ts*. This method cannot be considered to provide the absolute accuracy, because of the strong hypothesis in the calculations (non-correlation of errors or linearity of the error model). However, it tends to show that our retrieval is realistic and in good agreement with the independent LSA SAF estimates.

## 6. Conclusion and Perspectives

[90] A non-linear spectral emissivity interpolator has been built, essentially based on MODIS retrieval. This interpolator uses the six emissivities retrieved from the MODIS retrieval as inputs and provides as outputs the ten emissivity PCA components necessary to calculate the whole infrared spectrum at IASI spectral resolution. Comparison of radiative transfer calculations to IASI measurements showed very

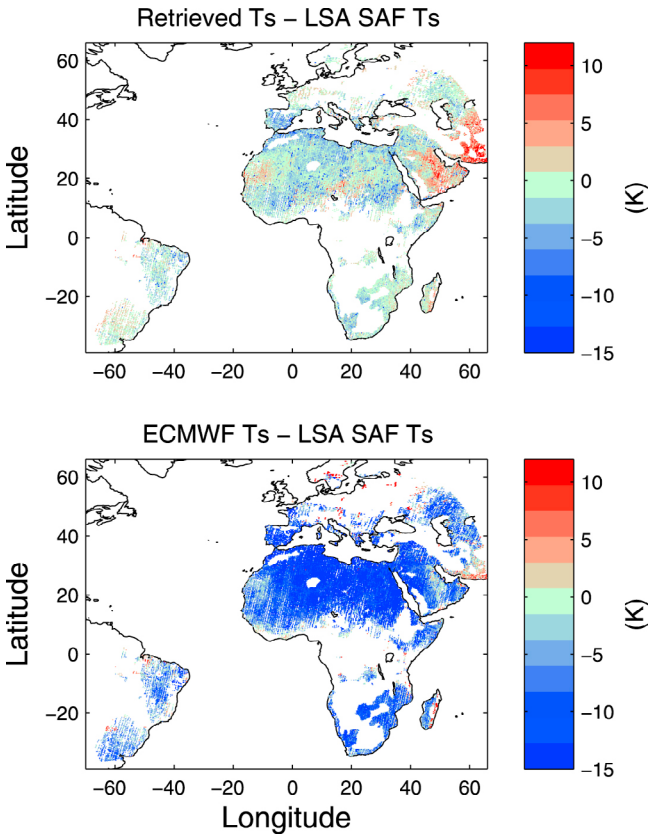


**Figure 12.** Retrieved (top) *Ts* minus LSA SAF *Ts* and (bottom) ECMWF *Ts* minus LSA SAF *Ts*. All data from the first week of January, April, July, and October are gathered on the map.

close results when using monthly estimates of the emissivity from different sources. However, improvement on the surface characterization is still necessary as the difference between measured and calculated BT using those monthly emissivities is higher in the "window" region than in channels only sensitive to the atmosphere. Comparing simulated and measured BT provides a good estimate of the quality of the emissivity and surface temperature information.

[91] The output from the emissivity interpolator is used as first guess in a physical inversion scheme that retrieves simultaneously the emissivity spectrum and the surface skin temperature. Radiative transfer calculation with the retrieved surface information shows great improvements. The differences with satellite measurements averaged over bands 1 and 2 of the IASI spectrum is 3.5 K using the first guessed surface information, 2.1 K using the retrieved *Ts* and the first guessed emissivity spectrum, and 1.7 K using the retrieved surface information. The retrieved surface skin temperatures are compared to the LSA SAF estimates derived from SEVIRI measurements and the root mean square difference is below 2 K. The emissivity spectra retrieved from this inversion can be used to build a dedicated climatology for IASI and AIRS applications.

[92] In the next step, an atmospheric profile retrieval will be developed. The surface inversion scheme from this study will be integrated to it. The knowledge of the surface characteristics will help the atmospheric retrieval, especially in the surface-sensitive channels that provide the information about the lower atmospheric layers. Simultaneous retrieval of surface and atmospheric characteristics will be performed.

[93] Finally, improvement of atmospheric retrievals could be achieved by combining infrared and microwave information in order to benefit from the synergy of these observations. In *Aires* [2011] and *Aires et al.* [2011b], the microwave/infrared synergy has been evaluated over ocean. The same work is to be performed over continental surfaces where the complexity of the retrieval process should benefit even more from the combination of observations in the two wavelength ranges.

[94] **Acknowledgments.** The authors would like to thank E. Borbas, D. K. Zhou, and the LSA SAF for their collaboration in this study or for providing their databases. The first author would also like to thank Hervé Le Treut and Laurence Picon for making this work possible. This work has been partly financed by the Université Pierre et Marie Curie and the Collège Des Ingénieurs through a PhD allowance to Maxime Paul.

## References

Aires, F. (2011), Measure and exploitation of multisensor and multiwavelength synergy for remote sensing: 1. Theoretical considerations, *J. Geophys. Res.*, *116*, D02301, doi:10.1029/2010JD014701.

Aires, F., C. Prigent, W. Rossow, and M. Rothstein (2001), A new neural network approach including first guess for retrieval of atmospheric water vapor, cloud liquid water path, surface temperature, and emissivities over land from satellite microwave observations, *J. Geophys. Res.*, *106*(D14), 14,887–14,907.

Aires, F., C. Prigent, F. Bernardo, C. Jiménez, R. Saunders, and P. Brunel (2011a), A Tool to Estimate Land-Surface Emissivities at Microwave frequencies (TELSEM) for use in numerical weather prediction, *Q. J. R. Meteorol. Soc.*, *137*, 690–699, doi:10.1002/qj.803.

Aires, F., M. Paul, C. Prigent, B. Rommen, and M. Bouvet (2011b), Measure and exploitation of multisensor and multiwavelength synergy for remote sensing: 2. Application to the retrieval of atmospheric temperature and water vapor from MetOp, *J. Geophys. Res.*, *116*, D02302, doi:10.1029/2010JD014702.

Capelle, V., A. Chédin, E. Péquignot, P. Schlüessel, S. M. Newman, and N. A. Scott (2012), Infrared continental surface emissivity spectra and skin temperature retrieved from IASI observations over the tropics, *J. Appl. Meteorol. Climatol.*, in press.

Caselles, V., E. Valor, C. Coll, and E. Rubio (1997), Thermal band selection for the prism instrument: 1. Analysis of emissivity-temperature separation algorithms, *J. Geophys. Res.*, *102*(D10), 11,145–11,164.

Chalon, G., F. Cayla, and D. Diebel (2001), IASI—An advanced sounder for operational meteorology, paper presented at the 52nd Congress of the International Astronautical Federation, Int. Astronaut. Fed., Toulouse, France, 1–5 Oct.

Eyre, J. (1991), A fast radiative transfer model for satellite sounding systems, *Res. Dep. Tech. Memo*, *176*, Eur. Cent. for Medium-Range Weather Forecasts, Reading, U. K.

Freitas, S., I. Trigo, J. Bioucas-Dias, and F. Göttsche (2010), Quantifying the uncertainty of land surface temperature retrievals from seviri/meteosat, *IEEE Trans. Geosci. Remote Sens.*, *48*(1), 523–534, doi:10.1109/TGRS.2009.2027697.

Hulley, G., and S. Hook (2009), The North American ASTER Land Surface Emissivity Database (NAALSED) Version 2.0, *Remote Sens. Environ.*, *113*, 1967–1975.

Hulley, G., S. Hook, E. Manning, S. Lee, and E. Fetzer (2009), Validation of the Atmospheric Infrared Sounder (AIRS) version 5 land surface emissivity product over the Namib and Kalahari deserts, *J. Geophys. Res.*, *114*, D19104, doi:10.1029/2009JD012351.

Janssen, P. A. E. M., S. Abdalla, H. Hersbach, and J. R. Bidlot (2007), Error estimation of buoy, satellite and model wave height data, *J. Atmos. Oceanic Technol.*, *24*, 1665–1677, doi:10.1175/JTECH2069.1.

Jiménez, C., J. Catherinot, C. Prigent, and J. Roger (2010), Relations between geological characteristics and satellite-derived infrared and microwave emissivities over deserts in northern Africa and the Arabian Peninsula, *J. Geophys. Res.*, *115*, D20311, doi:10.1029/2010JD013959.

Jolliffe, I. T. (2002), *Principal Component Analysis*, 2nd ed., Springer, New York.

Li, Z., J. Li, X. Jin, T. J. Schmit, and E. Borbas (2010), An objective methodology for infrared land surface emissivity evaluation, *J. Geophys. Res.*, *115*, D22308, doi:10.1029/2010JD014249.

Marsden, R. F. (1999), A proposal for a neutral regression, *J. Atmos. Oceanic Technol.*, *16*, 876–883.

Matricardi, M., F. Chevallier, and S. Tjemkes (2001), An improved general fast radiative transfer model for the assimilation of radiance observations, *Res. Dep. Tech. Memo.*, *345*, Eur. Cent. for Medium-Range Weather Forecasts, Reading, U. K.

Mira, M., E. Valor, R. Boluda, V. Caselles, and C. Coll (2007), Influence of soil water content on the thermal infrared emissivity of bare soils: Implication for land surface temperature determination, *J. Geophys. Res.*, *112*, F04003, doi:10.1029/2007JF000749.

Pequignot, E. (2006), Détermination de l'émissivité et de la température des surfaces continentales: Application aux sondeurs spatiaux HIRS et AIRS/IASI, PhD thesis, Ecole Polytechnique, Palaiseau, France.

Pequignot, E., A. Chedin, and N. A. Scott (2008), Infrared continental surface emissivity spectra retrieved from airs hyperspectral sensor, *J. Appl. Meteorol. Climatol.*, *47*, 1619–1633.

Prigent, C., F. Aires, and W. Rossow (2006), Land surface microwave emissivities over the globe for a decade, *Bull. Am. Meteorol. Soc.*, *87*, 1573–1584, doi:10.1175/BAMS-87-11-1573.

Prigent, C., E. Jaumouille, F. Chevallier, and F. Aires (2008), A parameterization of the microwave land surface emissivity between 19 and 100 GHz, anchored to satellite-derived estimates, *IEEE Trans. Geosci. Remote Sens.*, *46*, 344–352.

Rodgers, C. D. (2000), *Inverse Methods for Atmospheric Sounding: Theory and Practice*, 1st ed., World Sci., Hackensack, N. J.

Rumelhart, D. E., G. E. Hinton, and R. J. Williams (1986), *Learning Internal Representations by Error Propagation*, pp. 318–362, MIT Press, Cambridge, Mass.

Running, S. W., T. R. Loveland, and L. L. Pierce (1994), A vegetation classification logic based on remote sensing for use in global biogeochemical models, *Ambio*, *23*, 77–81.

Salisbury, J. W., A. Wald, and D. M. D'Aria (1994), Thermal-infrared remote sensing and Kirchoff's law: 1. Laboratory measurements, *J. Geophys. Res.*, *99*, 11,897–11,911.

Saunders, R., M. Matricardi, and P. Brunel (1999), An improved fast radiative transfer model for assimilation of satellite radiance observations, *Q. J. R. Meteorol. Soc.*, *125*, 1407–1425, doi:10.1256/smsqj.55614.

Seemann, S. W., E. E. Borbas, R. O. Knuteson, G. R. Stephenson, and H.-L. Huang (2008), Development of a global infrared surface emissivity database for application to clear sky retrievals from multispectral satellite radiance measurements, *J. Appl. Meteorol. Climatol.*, *47*, 108–123.

Stoffelen, A. (1998), Toward the true near-surface wind speed: Error modeling and calibration using triple collocation, *J. Geophys. Res.*, *103*(C4), 7755–7766.

Trigo, I., I. Monteiro, F. Olesen, and E. Kabsch (2008), An assessment of remotely sensed surface temperature, *J. Geophys. Res.*, *113*, D17108, doi:10.1029/2008JD010035.

Trigo, I., et al. (2011), The satellite application facility for land surface analysis, *Int. J. Remote Sens.*, *32*(10), 2725–2744, doi:10.1080/01431161003743199.

Uppala, S., et al. (2005), The era-40 re-analysis, *Q. J. R. Meteorol. Soc.*, *131*, 2961–3012.

Vogel, R. L., Q. Liu, Y. Han, and F. Weng (2011), Evaluating a satellite-derived global infrared land surface emissivity data set for use in radiative transfer modeling, *J. Geophys. Res.*, *116*, D08105, doi:10.1029/2010JD014679.

Wan, Z., and J. Dozier (1996), A generalised split-window algorithm for retrieving land-surface temperature from space, *IEEE Trans. Geosci. Remote Sens.*, *34*, 892–905.

Wan, Z., and Z.-L. Li (1997), A physics-based algorithm for retrieving land-surface emissivity and temperature from EOS/MODIS data, *IEEE Trans. Geosci. Remote Sens.*, *35*, 980–996, doi:10.1109/36.602541.

Yu, Y., J. L. Privette, and A. C. Pinheiro (2008), Evaluation of split-window land surface temperature algorithms for generating climate data records, *IEEE Trans. Geosci. Remote Sens.*, *46*(1), 179–192.

Zhou, D. K., A. M. Larar, X. Liu, W. L. Smith, L. L. Strow, P. Yang, P. Schlüssel, and X. Calbet (2011), Global land surface emissivity retrieved from satellite ultraspectral IR measurements, *IEEE Trans. Geosci. Remote Sens.*, *49*, 1277–1290, doi:10.1109/TGRS.2010.2051036.